Mitigating SOX2-potentiated Immune Escape of Head and Neck Squamous Cell Carcinoma with a STING-inducing Nanosatellite Vaccine

Yee Sun Tan[1,2], Kanokwan Sansanaphongpricha[2,3], Yuying Xie[4], Christopher R. Donnelly[5], Xiaobo Luo[1,6], Blake R. Heath[1,7], Xinyi Zhao[1], Emily Bellile[2], Hongxiang Hu[3], Hongwei Chen[3], Peter J. Polverini[1,2], Qianming Chen[6], Simon Young[8], Thomas E. Carey[2,9], Jacques E. Nör[2,9,10], Robert L. Ferris[11], Gregory T. Wolf[2,9], Duxin Sun[2,3], and Yu L. Lei[1,2,5,7,9]

Abstract

Purpose: The response rates of Head and Neck Squamous Cell Carcinoma (HNSCC) to checkpoint blockade are below 20%. We aim to develop a mechanism-based vaccine to prevent HNSCC immune escape.

Experimental Design: We performed RNA-Seq of sensitive and resistant HNSCC cells to discover central pathways promoting resistance to immune killing. Using biochemistry, animal models, HNSCC microarray, and immune cell deconvolution, we assessed the role of SOX2 in inhibiting STING-type I interferon (IFN-I) signaling-mediated antitumor immunity. To bypass SOX2-potentiated STING suppression, we engineered a novel tumor antigen–targeted nanosatellite vehicle to enhance the efficacy of STING agonist and sensitize SOX2-expressing HNSCC to checkpoint blockade.

Results: The DNA-sensing defense response is the most suppressed pathway in immune-resistant HNSCC cells. We identified SOX2 as a novel inhibitor of STING. SOX2 facilitates autophagy-dependent degradation of STING and inhibits IFN-I signaling. SOX2 potentiates an immunosuppressive microenvironment and promotes HNSCC growth *in vivo* in an IFN-I-dependent fashion. Our unique nanosatellite vehicle significantly enhances the efficacy of STING agonist. We show that the E6/E7–targeted nanosatellite vaccine expands the tumor-specific CD8^{+} T cells by over 12-fold in the tumor microenvironment and reduces tumor burden. A combination of nanosatellite vaccine with anti-PD-L1 significantly expands tumor-specific CTLs and limits the populations expressing markers for exhaustion, resulting in more effective tumor control and improved survival.

Conclusions: SOX2 dampens the immunogenicity of HNSCC by targeting the STING pathway for degradation. The nanosatellite vaccine offers a novel and effective approach to enhance the adjuvant potential of STING agonist and break cancer tolerance to immunotherapy. *Clin Cancer Res; 24(17); 4242–55. ©2018 AACR.*

[1]Department of Periodontics and Oral Medicine, The University of Michigan School of Dentistry, Ann Arbor, Michigan. [2]University of Michigan Rogel Cancer Center, Ann Arbor, Michigan. [3]Department of Pharmaceutical Sciences, the University of Michigan College of Pharmacy, Ann Arbor, Michigan. [4]Department of Computational Mathematics, Science, and Engineering, Michigan State University, East Lansing, Michigan. [5]Oral Health Sciences PhD Program, The University of Michigan School of Dentistry, Ann Arbor, Michigan. [6]State Key Laboratory of Oral Diseases, West China School of Stomatology, Sichuan University, Chengdu, China. [7]Graduate Program in Immunology, The University of Michigan Medical School, Ann Arbor, Michigan. [8]The University of Texas Health Science Center at Houston, School of Dentistry, Houston, Texas. [9]Department of Otolaryngology – Head and Neck Surgery, the University of Michigan Health System, Ann Arbor, Michigan. [10]Department of Cariology, Restorative Sciences, and Endodontics, the University of Michigan School of Dentistry, Ann Arbor, Michigan. [11]Department of Otolaryngology, University of Pittsburgh Cancer Institute, The University of Pittsburgh School of Medicine, Pittsburgh, Pennsylvania.

Note: Supplementary data for this article are available at Clinical Cancer Research Online (http://clincancerres.aacrjournals.org/).

Y.S. Tan and K. Sansanaphongpricha contributed equally to this article.

Corresponding Authors: Yu L. Lei, University of Michigan-Ann Arbor, 1600 Huron Parkway 2355, Ann Arbor, MI 48109. Phone: 734-615-6967; Fax: 734-763-5503; E-mail: leiyuleo@med.umich.edu; and Duxin Sun, duxins@med.umich.edu

doi: 10.1158/1078-0432.CCR-17-2807

©2018 American Association for Cancer Research.

Introduction

The traditional treatment of patients with head and neck squamous cell carcinoma (HNSCC) is often associated with significant morbidity (1, 2). Monoclonal antibodies (mAbs) blocking the immune checkpoint receptors (ICR) have shown promises by restoring exhausted cytotoxic T lymphocyte (CTL) function in the tumor microenvironment (TME; ref. 3). However, less than 20% of HNSCC patients, regardless of the human papillomavirus (HPV) status, could benefit from this regimen (4). One major limitation of the current immunotherapies is the lack of strategies for "cold" cancers, which are hypoimmunogenic and exhibit low tumor-specific CTL among tumor-infiltrating lymphocytes (TIL). Thus, there is a pressing need to identify the mechanisms that dampen HNSCC immunogenicity and develop novel strategies for cold tumors (5, 6).

The success of ICR depends on a collection of tumor-specific CTL in the TME, but cold tumors demonstrate a poor infiltration of effectors. Thus, new approaches to expand the tumor-specific CTLs are highly promising to break tumor immune tolerance. Recent evidence suggests that type I interferon (IFN-I) signaling in the TME promotes CD8^{+} CTL production in melanoma and fibrosarcoma models (7–9). The induction of IFN-I is mediated by pattern recognition receptors (PRR),

AACR

Translational Relevance

Despite the promise checkpoint blockade has brought to the clinics, this treatment is ineffective in over 80% of HNSCC patients. A major challenge is that HNSCC often develops resistance to immunity and exhibits a poor infiltration of T cells. This study characterizes the transcriptomic alterations when HNSCC cells become resistant to immune effectors. We delineate a novel SOX2–STING signaling axis that bridges intrinsic oncogenic signaling with suppression of antitumor immune response. SOX2 shows a previously unrecognized role in potentiating tumor immune escape by eliciting autophagy-dependent degradation of STING and thereafter rendering an immunosuppressive tumor microenvironment. Anticancer vaccine offers a promising solution to prevent immune escape driven by STING suppression. Hence, we engineered a nanosatellite vaccine delivery vehicle that significantly enhances the adjuvant potential of STING agonist. A combination of nanosatellite vaccine with checkpoint blockade effectively controls tumor growth by expanding tumor-specific T-cell repertoire and reducing populations expressing markers for functional exhaustion.

including DNA sensors such as cyclic GMP-AMP synthase (cGAS). DNA-bound cGAS generates a second messenger cyclic GMP-AMP (cGAMP) to activate the adaptor protein stimulator of IFN genes (STING), which promotes IFN-I (10, 11). IFN-I target genes include a number of Th1 chemokines, such as CXCL9 and CXCL10, which are critical for the tumor-homing of antigen-presenting cells (APC) and effectors (12), but STING is often inhibited in cancers, and the mechanisms are insufficiently characterized. Thus, identification of the inhibitory pathways of STING in HNSCC will provide new mechanistic insight into its resistance to immune killing.

Although restoration of IFN-I signaling in the TME is an attractive strategy, the use of recombinant IFN-α or IFN-β is hampered by their short half-lives (∼5 hours). STING agonist cGAMP has shown immune-priming potential (13), and it needs to be delivered to the cytoplasm to be effective, but this has been challenging due to its hydrophilic structure. Thus, better delivery systems for this immune adjuvant will address a major technical barrier to more effectively expand tumor-specific CTLs. Nanoparticles represent an ideal vehicle to deliver antigens and vaccine adjuvant: (i) in comparison with a soluble formulation, nanoparticles improve the pharmacodynamics of vaccine components and increase their uptake by APC; and (ii) as antigen density controls the efficiency of APC cross-priming (14), nanoparticles can be engineered to present enhanced surface area and deliver high-density antigens.

In this study, we discovered a novel function of an HNSCC oncoprotein SOX2 in blocking STING-mediated IFN-I activation. As a mechanism, SOX2 potentiates STING degradation in an autophagy-dependent fashion. Using a syngeneic mouse model and clinical specimens, we found that SOX2 dampens antitumor immunity. To restore IFN-I signaling in the TME, we engineered a nanosatellite vehicle to deliver cGAMP and HPV16 E6/E7 peptides. The nanosatellite vaccine significantly expands the tumor-specific CTL repertoire and sensitizes cold tumors to an

ICR inhibitor. A combination of nanosatellite vaccine with anti-PD-L1 not only promotes CD8+ CTL but also reduces CTL exhaustion, delivering superior protection.

Materials and Methods

Cell culture

HPV− PCI-13 was obtained from the University of Pittsburgh (Pittsburgh, PA). HPV− UMSCC22b and HPV+ UMSCC47 were established at the University of Michigan (Ann Arbor, MI). HPV− FaDu and HEK-293T were from ATCC. The HNSCC lines were authenticated and tested for mycoplasma from their source (15). The human HNSCC and HEK-293T cells were maintained in DMEM containing 10% FBS, GlutaMAX (Gibco), 100 U/mL penicillin, and 100 mg/mL streptomycin. MOC2-E6/E7 cells were obtained from the Harvard University and maintained in Iscove's modified Dulbecco's medium/F12 (2:1) with 5% FBS, penicillin/streptomycin, 5 ng/mL EGF (Millipore), 40 ng/mL hydrocortisone, 5 μg/mL insulin, and 4 μg/mL puromycin. The reporter THP1-blue ISG cells were obtained from InvivoGen and cultured in complete RPMI1640 medium supplemented with 10% FBS, GlutaMAX (Gibco), 100 U/mL penicillin, and 100 mg/mL streptomycin. Bone marrow–derived dendritic cells (BMDC) were isolated from 8-week-old C57BL/6 mice and cultured in complete RPMI1640 with nonessential amino acid, sodium pyruvate, 2-mercaptoethanol, and 10 ng/mL GM-CSF (PeproTech).

Coculture of HNSCC cells with effector cells

Peripheral blood monocytes were separated from buffy coats of two healthy donors using Ficoll–Paque gradient. Primary human NK and CD8+ T cells were separated using NK-cell CD8+ T-cell enrichment kits, respectively (catalog nos. 19055 and 19053, StemCell Technologies), and cultured in complete RPMI1640 medium. HNSCC cells were cocultured with the primary NK cells in the presence of 5 μg/mL cetuximab (Bristol–Myers Squibb). Dead tumor cells and old NK cells were washed off each week before replenishing with fresh NK cells for 12 times. HLA-A*0201–restricted EGFR-specific CD8+ CTLs were generated as reported previously (16). Wild-type and resistant PCI-13 cells were labeled with CFSE prior to coculture with NK cells or CTL, and flow cytometric analysis of 7-AAD (catalog no. 559925, BD Biosciences) staining was performed to assess percent tumor cell death.

RNA-Seq and pathway enrichment analysis

Next-generation sequencing of paired-end 50 nt reads was performed using the poly A–based libraries at the U-M DNA Sequencing Core. Result reads were mapped to the hg19 genome assembly using MapSplice v2.1.6, and gene expression was quantified using RSEM and normalized within sample. An R package, edgeR, was used to identify the genes that are differentially expressed among cell lines, and the top 2,000 most significant genes were selected for gene set enrichment analysis. Raw data files and processed data files are available through the NCBI Gene Expression Omnibus (GEO) record GSE100828.

Quantitation of gene expression

Gene expression qPCR primers are: *IFNB1* F 5′-CATTACCT-GAAGGCCAAGGA, R 5′-CAATTGTCCAGTCCCAGAGG; *CXCL9* F 5′-GTGGTGTTCTTTTCCTCTTGGG, R 5′-ACAGCGACCCTTTCT-CACTAC; *CXCL10* F 5′-CTCCAGTCTCAGCACCATGA, R 5′-

GCTCCCCTCTGGTTTTAAGG; *ISG15* F 5′-CTGAGAGGCAGCGA-ACTCAT, R 5′-AGCATCTTCACCGTCAGGTC; *ISG54* F 5′- ACGG-TATGCTTGGAACGATTG, R 5′-AACCCAGAGTGTGGCTGATG; *IFNA4* F 5′-CCTAGAGGCCGAAGTTCAAG, R 5′-TTGTGCCAG-GAGTATCAAGG; *SOX2* F 5′-CCCACCTACAGCATGTCCTACTC, R 5′-TGGAGTGGGAGGAAGAGGTAAC; *STAT3* F 5′-TGAGACT-TGGGCTTACCATTGGGT, R 5′-TCTTTAATGGGCCACAACAG-GGCT; *STAT1* F 5′-GAGCAGGTTCACCAGCTTTATGAT, R 5′-AACGGATGGTGGCAAATGA; *NLRX1* F 5′-AGCTGCTATCATC-GTCAAC, R 5′-ACCGCAGATCTCACCATAG; *NLRC3* F 5′-GTG-CCGACCGACTCATCTG′, R 5′-GTCCTGCACTCATCCAAGC; *HPRT1* F 5′- ATGCTGAGGATTTGGAAAGG, R 5′-CAGAGGGCTA-CAATGTGATGG; *Ifnb1* F 5′-CCAGCTCCAAGAAAGGACGA, R 5′-CGCCCTGTAGGTGAGGTTGAT; *pan-Ifna* F 5′-CCTGAGAGAGA-AACACAGCC, R 5′-TCTGCTCTGACCACYTCCCAG; *Cxcl9* F 5′-GAGCAGTGTGGAGTTCGAGG, R 5′-TCCGGATCTAGGCAGGT-TTG; *Cxcl10* F 5′-AATGAGGGCCATAGGGAAGC, R AGCCATC-CACTGGGTAAAGG; *Mx1* F 5′-TCTGAGGAGAGCCAGACGAT′, R 5′-ACTCTGGTCCCCAATGACAG; *Ifng* F 5′-CGGCACAGTCA-TTGAAAGCCTA, R 5′-GTTGCTGATGGCCTGATTGTC; *Trex1* F 5′-CGTCAACGCTTCGATGACA, R 5′-AGTCATAGCGGTCAC-CGTT; *Hprt1* F 5′-GATTAGCGATGATGAACCAGGTT, R 5′-CCTCCCATCTCCTTCATCACA.

Plasmids, retroviruses, CRISPR-Cas9 lentiviruses, transfection, and reporter assays

STING expression plasmid was from Dr. Glen N. Barber at the University of Miami. ISRE luciferase reporter, retroviral, and lentiviral packaging vectors were from Dr. Jenny P.-Y. Ting at the University of North Carolina at Chapel Hill. pEGFP-LC3 (#24920), pLXSN16E6E7 (#52394), pMXs-Sox2 (#13367) and lentiCRISPRv2 (#98290) were from Addgene. The sgRNA targeting *SOX2* is 5′-ATTATAAATACCGGCCCCGG. Cells were about 70% confluent prior to transfections with Lipofectamine 2000 (catalog no. 11668019, Thermo Fisher Scientific) as reported previously (17). Luciferase assay was performed as described (17). Supernatants from THP-1-blue ISG reporter cells were incubated with Quanti-Blue (InvivoGen) to measure IFN activation.

Immunoblots and IHC

The antibodies include phospho-TBK1 (Ser172; catalog no. 5483S, Cell Signaling Technology), TBK1 (catalog no. 3504S, Cell Signaling Technology), phospho-p65 (Ser536; catalog no. 3033S, Cell Signaling Technology), SOX2 (catalog no. 23064, Cell Signaling Technology), STING (catalog no. 13647, Cell Signaling Technology), LC3B (catalog no. 2775, Cell Signaling Technology), p65 (catalog no. PA1-186, Thermo Fisher Scientific), HPV16E7 (catalog no. sc-65711, Santa Cruz Biotechnology), β-actin (catalog no. ab49900, Abcam), goat anti-rabbit IgG H&L (HRP; catalog no. Ab97051, Abcam). Densitometry was performed using ImageJ. The IHC antibodies include Mx1 (1:300 dilution, catalog no. HPA030917-100UL, Sigma-Aldrich), and Sox2 (1:300, catalog no. 23064, Cell Signaling Technology).

TIL separation and flow cytometry

Excised tumors were minced into pieces, and then dissociated by passing through a 70-μm cell strainer to obtain single-cell suspension. Spleens were processed by mechanical dissociation, followed by lysis of red blood cells (catalog no. A10492-01, Gibco). Ficoll-Paque PLUS (catalog no. 17-1440-03, GE Healthcare Life Sciences) was added to the bottom of the conical tubes containing single-cell suspension in RPMI1640. Density-gradient centrifugation was performed to purify immune cells. Rare sample with inadequate number of TILs was excluded from further processing. Flow cytometry antibodies include: CD3 (17A2, BD Biosciences), CD4 (RM4-5, BioLegend), CD8 (53-6.7, BioLegend), CD366 (RMT3-23, BioLegend), CD279 (29F.1A12, BioLegend), CD16/32 (93, eBioscience), MHC-class II (M5/114.15.2, eBioscience), CD86 (GL1, eBioscience), tetramer recognizing HLA-A*0201–restricted EGFR 854L. ILDFGLAKL (NIH tetramer core), tetramer recognizing H-2D[b]–restricted HPV16 E7 epitope RAHYNIVTF (NIH tetramer core), and viability dye (catalog no. 65-0865-14, eBioscience). All data were analyzed using FlowJo software.

Formulation of SatVax and peptide vaccine in montanide

The iron oxide (IONP) core particles of the nanosatellites were synthesized by thermal decomposition as described previously (19). The core particles were coated by a diblock copolymer (PEO-*b*-γMPS), and added into Au$_2$SNP (2 nm) solution. Nanoparticles were characterized by transmission electron microscope. The peptides are E6$^{43-57}$ Q15L (CSKKK-QLLRREVYDFAFRDL), E7$^{49-57}$ R9F (CSKKK-RAHYNIVTF), and E7$^{44-62}$ Q19D (CSKKK-QAEPDRAHYNIVTFCCKCD; Elim Biopharmaceuticals). The nanosatellites conjugated with peptides were purified by magnet separator, and incubated with 2′3′ cGAMP. Hydrodynamic diameters were measured by Zeta Sizer (Malvern Instruments). To produce a peptide vaccine, E6/E7 peptides were emulsified in clinical-grade montanide-ISA51 (SEPPIC Inc).

Animals

Syngeneic HNSCC cells were implanted subcutaneously at the neck of 6- to 8-week-old C57BL/6 or *Ifnar1*$^{-/-}$ mice (Jackson Laboratory). Tumor volume was calculated as $^{1}/_{2}$(length × width^2). In the irradiation experiments, mice were irradiated with a single 20-Gy dose or three fractionated doses of 8-Gy when tumors reached approximately 200 mm^3. For MRI, nanosatellite conjugated with E7 peptides were administered subcutaneously at tail base at the 50 μg iron/mouse prior to imaging. To test the vaccines, mock (PBS, 100 μL), 2′3′-cGAMP (50 μg/100 μL; catalog no. tlrl-nacga23-1, InvivoGen), peptides (18.5 nmol/100 μL), or 3 weekly doses of SatVax [2′3′ cGAMP (50 μg) and peptide (18.5 nmol/L) conjugated with the nanosatellite/100 μL] was administered subcutaneously at tail base. Intraperitoneal injections of anti-PD-L1 (100 μg/100 μL; clone B7H1, BioXCell) were performed on day 1 and 4 after each vaccination with a total of 6 doses. For vaccination in hosts with established tumors, montanide-E6/E7 peptide emulsion (100 μL/mouse), SatVax, or PBS-mock was administered at tail base when tumors reached approximately 200 mm^3. All animal work was done in accordance with and approved by the Institutional Animal Care and Use Committee (PRO00006591).

Clinical samples

Institutional review boards were approved by the University of Michigan (HUM00042189 and HUM00113038). Primary HNSCC specimens were procured from 195 patients through the University of Michigan Head and Neck Cancer

Program, with demographic information summarized in Supplementary Table S2. Three representative cores were extracted from each tumor and built into tissue microarrays (TMA). Tumor parenchyma was defined by a pathologist, and IHC staining was quantitated using Aperio ImageScope as reported previously (18). Scores for each patient were averaged from three cores. Occasional cores with inadequate tumor tissue were excluded.

Statistical analysis

Differences among groups were examined by ANOVA followed by multiple comparison tests. Comparisons between two independent groups were made by unpaired t test, two-sided. Differences in tumor growths among treatment groups were assessed by the Generalized Estimating Equations model. Differences in survival were assessed by Kaplan–Meier curves and a log-rank test. We performed power analysis based on our pilot experiments to decide the number of animals. Immune subsets deconvolution using RNA-Seq data was performed using CIBERSORT as reported previously (20). All experiments were repeated 2 to 3 times. All values shown represent mean ± SEM.

Results

The DNA-sensing defense response promotes HNSCC sensitivity to effector immune cells

Recent high-throughput screen suggests that tumor–immune cell coculture can be utilized to discover central pathways driving cancer resistance to effectors (21). To reveal mechanisms underpinning HNSCC resistance to immune killing, we incubated HNSCC cells with primary human natural killer (NK) cells. As primary NK cells do not efficiently kill target HNSCC cells without antibody opsonization, we added a low dose of EGFR-targeted cetuximab, which alone does not show any cytotoxic effects (18). After HNSCC-NK coculture was repeated 12 times, we noticed that these HNSCC cells become resistant when challenged with NK cells at different target: effector (T:E) ratios (Fig. 1A). Although effectors such as NK and $CD8^+$ CTLs utilize different mechanisms to recognize cancer cells, they can sense the same Th1 chemokines to gain proximity to tumor cells and deliver the same cytotoxic granzymes into targets (22). Hence, we tested whether NK-resistant HNSCC cells can develop broad resistance to the two major immune effectors. We separated $CD8^+$ T cells from an HLA-matched donor, and generated HLA-A*0201–restricted EGFR-specific CTL (Supplementary Fig. S1A and S1B). We incubated the CTLs with HNSCC cells, and found that the NK-resistant tumor cells are also resistant to CTL (Fig. 1B).

To identify central pathways that drive broad cancer resistance to effectors, we performed RNA-Seq of the wild-type and immune-resistant HNSCC cells (GSE100828). A gene set enrichment analysis (GESA) identified the most significantly altered pathways, which include defense response, cancer cell inflammatory signaling, and cell proliferation and death pathway (q < 0.01; Fig. 1C). The defense response is mainly constituted of the IFN-I signatures. We cross referenced the significantly altered genes with genes in the Interferome database (23), and found that the expression profiles of 358 IFN-I-regulated genes are contrasted between wild-type and resistant cells. The IFN-stimulated genes (ISG) are significantly inhibited in immune-resistant cancer cells (Fig. 1D). ISGs include Th1 chemokines, such as CXCL10,

which recruit APC and effectors to the tumor bed (7, 12). Multiple proteins that dampen STING-mediated IFN-I signaling, such as NLRX1 and NLRC3 (17, 24), are increased in resistant cells (Fig. 1E; Supplementary Table S1). Utilizing qPCR, we verified the altered expression levels of representative regulators of IFN signaling between immune-sensitive and -resistant HNSCC cells (Fig. 1F–K).

SOX2 inhibits STING-mediated activation of the DNA-sensing pathway

To better understand how oncogenic signaling potentiates immune escape by targeting the IFN-I pathway, we next sought to explore the regulatory mechanism of STING-mediated IFN-I induction in HNSCC. SOX2 promotes the development of squamous cell carcinomas including HNSCC (25–29). Interestingly, SOX2 is also significantly upregulated when cancer cells become resistant to effector cells (Fig. 1E and F). To investigate whether SOX2 has a previously unknown function in regulating inflammation, we first assessed whether SOX2 regulates STING signaling in HEK-293T cells, which is a well-characterized model for IFN signaling. HEK-293T cells are free of somatic mutations, whereas HNSCC cell lines harbor mutations that may potentially affect the regulatory network of IFN-I signaling. In addition, STING and its regulators, such as NLRX1 and NLRC3, were initially discovered in HEK-293T cells (10, 24, 30). We first transfected SOX2 expression plasmid in HEK-293T cells and assessed whether it modulates PRR-induced IFN-sensitive response element (ISRE) promoter activation. We found that SOX2 expression inhibits STING- and B-DNA poly(dA:dT)-induced ISRE activation in a dose-dependent fashion (Fig. 2A and B). SOX2 also inhibits MAVS-induced ISRE activation (Fig. 2C), suggesting that SOX2 has a broad inhibitory effect on the intracellular PRR-mediated IFN-I signaling. In agreement, SOX2 potently suppresses STING- and poly(dA:dT)-induced transcription of IFNB1 and an IFN-I-target gene CXCL10 in HEK-293T cells (Supplementary Fig. S2A). To validate our findings in HNSCC cells, we screened a panel of HNSCC cell lines, and found that UMSCC47 and UMSCC22b cells exhibit low endogenous levels of SOX2 expression. Hence, we expressed SOX2 in these two cell lines, and recapitulated the findings we observed in HEK-293T cells (Fig. 2D and E). PCI-13 cells have a higher level of SOX2 expression. Thus, we generated a CRISPR-Cas9 lenti-virus to produce $SOX2^{-/-}$ PCI-13 as a loss-of-function approach (Supplementary Fig. S2B). Consistently, SOX2 deficiency enhances the transcript of IFNB1 in response to STING agonist cGAMP and intracellular DNA challenge (Fig. 2F and G).

To confirm the findings with mRNA, we examined the activation markers of IFN-I using immunoblots. STING promotes the phosphorylation of TBK1 (S172) and p65 (S536), and SOX2 potently suppresses STING-induced phosphorylation of TBK1, and to a lesser extent for p65 in HEK-293T, UMSCC47 and UMSCC22b cells (Fig. 2H; Supplementary Fig. S2C and S2D). Interestingly, we noticed that SOX2 decreases the protein levels of STING (Fig. 2H; Supplementary Fig. S2D). STING is a known cargo for autophagosomes (31). Thus, we examined whether SOX2 has an unrecognized role in autophagy induction as a mechanism of inhibiting STING. We found that SOX2 promotes autophagosome formation (Supplementary Fig. S2E) and autophagic flux (Fig. 2I; Supplementary Fig. S2F), increasing the turnover of LC3-II and STING.
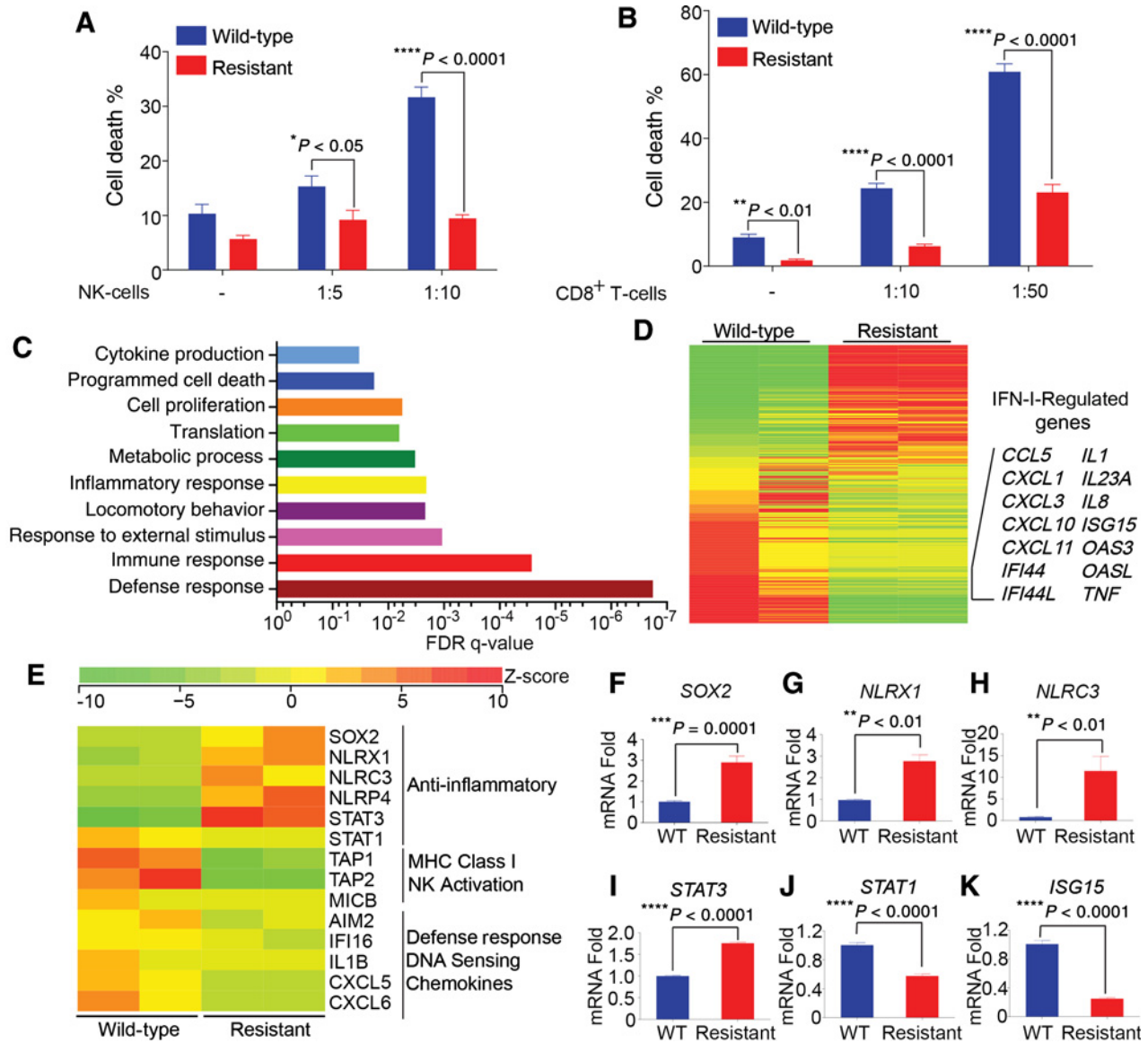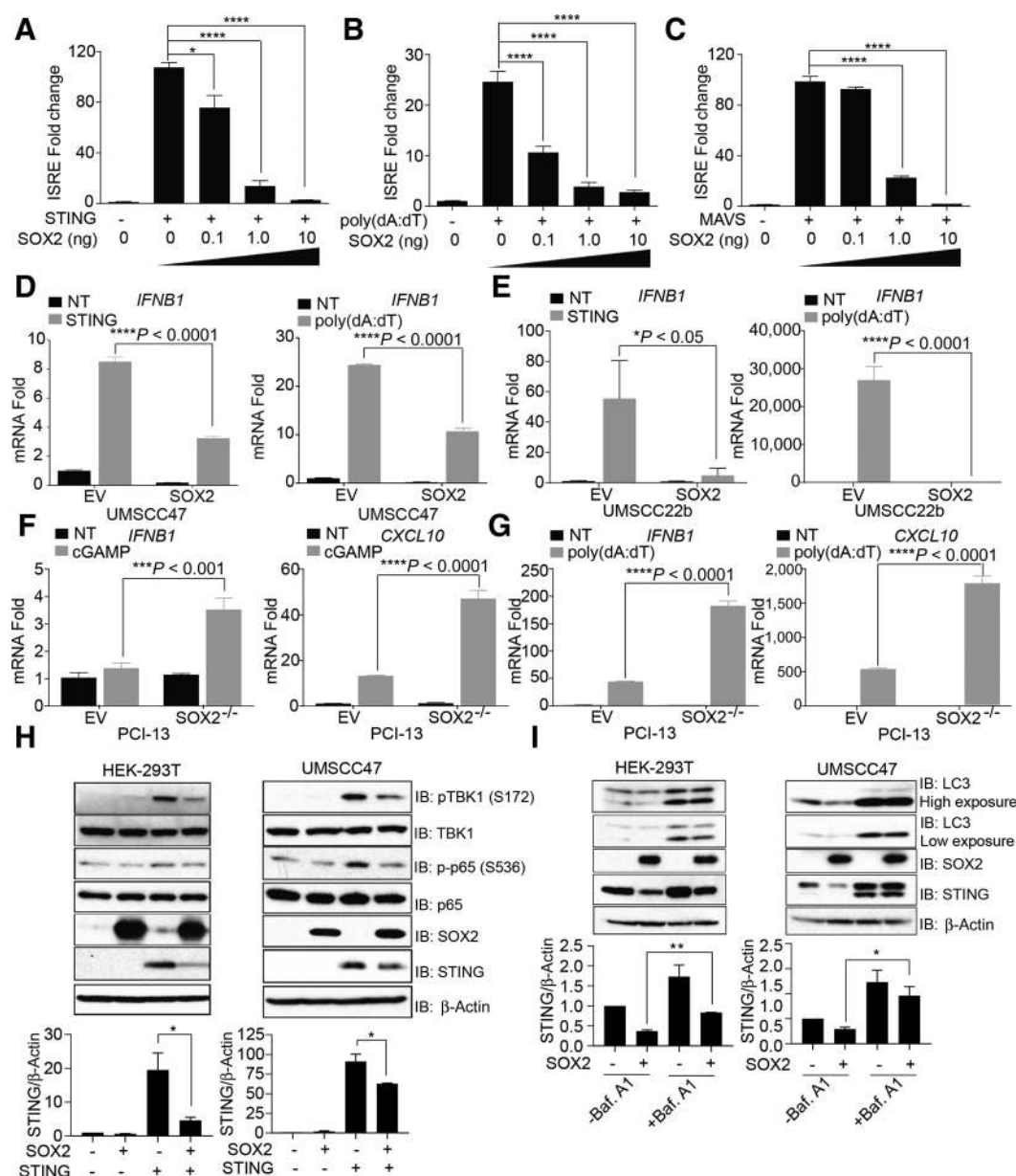
Figure 1.

Type I IFN signaling regulates tumor resistance to effector immune cells. **A,** PCI-13 cells were cocultured with NK cells isolated from 2 healthy donors in the presence of 5 µg/mL cetuximab. NK cells were replaced weekly for a total of 12 cycles of coincubation. Wild-type tumor cells and resistant cells were incubated with NK cells at two different T:E ratios for 16 hours. Flow cytometric analysis of 7-AAD staining was performed to assess percent tumor cell death. Each group contains three independent biologic replicates, mean ± SEM. Comparisons were made using two-way ANOVA followed by Bonferroni posttest. **B,** HLA-matched EGFR-specific CD8^{+} T cells were incubated with wild-type or NK-resistant tumor cells at two different T:E ratios for 16 hours. Flow cytometric analysis of 7-AAD staining was performed to assess percent tumor cell death. Each group contains three independent biologic replicates, mean ± SEM. Comparisons were made using two-way ANOVA followed by Bonferroni posttest. **C,** Gene set enrichment analysis (GSEA) of the significantly differentially expressed genes between the wild-type and resistant HNSCC cells (q value < 0.01). Ten of the most significantly altered pathways were shown. **D,** Significantly altered genes between sensitive and resistant HNSCC cells were cross-referenced in the Interferome database. A total of 358 IFN-regulated genes were significantly changed ($P < 0.05$). **E,** Heatmap of representative genes expression between wild-type and resistant cells. Plotted Z-score = (expression value of each mRNA−mean value for the same mRNA across all samples)/SD. List of additional differentially expressed genes can be found in Supplementary Table S1. **F–K,** qPCR was performed to validate candidate genes that were potentially altered when cancer became resistant to effector immune cells. Results represent mean ± SEM in technical triplicates, and comparisons were made using unpaired two-tailed t test.

Inhibition of autophagy by bafilomycin A1 partially restores LC3-II and STING levels, suggesting that SOX2-mediated degradation of STING is autophagy-dependent (Fig. 2I; Supplementary Fig. S2F).

Sox2 potentiates an immunosuppressive TME by inhibiting IFN-I signaling

To better understand the role of Sox2 in modulating TME *in vivo*, we developed a unique HPV16 E6/E7-expressing HNSCC

Figure 2.
SOX2 inhibits intracellular pattern recognition receptor-mediated IFN-I signaling. **A–C,** HEK-293T cells were transfected with an ISRE luciferase reporter construct and titrating doses of SOX2, in the presence of STING (**A**), poly(dA:dT) (**B**), or MAVS (**C**). ISRE promoter activity was quantitated by luciferase assay. Values are expressed as mean ± SEM of three biological repeats. One-way ANOVA with Tukey multiple comparisons test was performed for statistical analysis. *, $P < 0.05$; ****, $P < 0.0001$. **D,** UMSCC47 cells were challenged with STING or poly(dA:dT) for 16 hours in the absence or presence of SOX2. *IFNB1* mRNA levels were examined via qPCR. Values are expressed as mean ± SEM of three biologic replicates, and comparisons were made using unpaired t test. **E,** UMSCC22b cells were challenged with STING or poly(dA:dT) in the absence or presence of SOX2 expression, and assessed for *IFNB1* transcript via qPCR. Values are expressed as mean ± SEM of three biologic replicates, and comparisons were made using unpaired t test. **F,** Empty vector (EV) control and *SOX2*-targeted CRISPR-Cas9 lentiviruses were used to generate stable EV and *SOX2*-deficient PCI-13 cells, which were then transfected with the STING agonist cGAMP for 16 hours. *IFNB1* and *CXCL10* expression levels were examined via qPCR. Values are expressed as mean ± SEM of three biologic replicates, and comparisons were made using unpaired t test. **G,** EV and *SOX2*-deficient PCI-13 cells were challenged with poly(dA:dT) for 16 hours, and assessed for *IFNB1* and *CXCL10* mRNA via qPCR. Values are expressed as mean ± SEM of three biologic replicates, and comparisons were made using unpaired t test. **H,** Representative immunoblots of HEK-293T and UMSCC47 cells transfected with the indicated plasmids are shown. Protein lysates were harvested 16 hours posttransfection and immunoblotted against the indicated IFN-I activation markers. Densitometry of STING/β-actin shown in the lower panel is quantitated using ImageJ. Additional densitometry analysis can be found in Supplementary Fig. S2C. $n = 2$ biological replicates, and results represent mean ± SEM. One-way ANOVA with Tukey multiple comparisons test was performed, *, $P < 0.05$. **I,** HEK-293T and UMSCC47 cells were transfected with STING in the absence or presence of SOX2 for 48 hours, and half of the group received 200 nmol/L bafilomycin A1 for 8 hours. The cell lysates were immunoblotted with the indicated antibodies, and quantitative densitometry of STING/β-actin is shown below. Immunoblots represent 2–3 biological repeats. Comparison of densitometric quantitation is made using unpaired t test and shown in the lower panels and Supplementary Fig. S2F. Results represent mean ± SEM (*, $P < 0.05$; **, $P < 0.01$).

model in immunocompetent hosts. The MOC2 cell line exhibits similar mutations as human HNSCC (32). We produced the MOC2-E6/E7 cell line by transducing the MOC2 cells with a retrovirus expressing HPV16 E6/E7 proteins (Supplementary Fig. S3A). MOC2-E6/E7 cells exhibit a low endogenous level of Sox2. We produced empty vector control and Sox2-expressing MOC2-E6/E7 cells using retroviruses (Supplementary Fig. S3B). Although the empty vector control and Sox2-expressing tumor cells show similar proliferation rates *in vitro*, Sox2-expressing tumors grow significantly more aggressively in C57BL/6 hosts (Supplementary Fig. S3C; Fig. 3A). IHC examination of Sox2-expressing tumors (Fig. 3B, top) reveals histologic similarity to SOX2$^+$ human HNSCC with a diffuse strong nuclear staining pattern (Fig. 3B, bottom; ref. 33).

Ionizing radiation (IR) has been characterized as an immunity-inducing strategy, which depends on STING-mediated IFN-I signaling (34). Hence, we similarly treated MOC2-E6/E7 tumors with 20-Gy IR to assess whether Sox2 dampens IR-induced immune activation. Sox2-expressing tumors exhibit larger tumor volumes with or without IR (Fig. 3A), and we did not see IR-induced upregulation of IFN signature gene transcripts in the TME (Fig. 3C–F). High levels of Sox2 significantly dampen intrinsic host immune activation (Fig. 3C–F). IHC assessment of the tumors shows that the expression levels of an IFN-I-inducible protein Mx1 are reduced in Sox2-expressing tumors (Supplementary Fig. S4A). Using tumor tissue homogenates, we found that the phosphorylation of Tbk1 and p65 in Sox2-positive tumors are lower than those in the control tumors (Fig. 3G; Supplementary Fig. S4B and S4C). Consistent with its role in promoting Sting degradation, Sox2-expressing tumors also exhibit lower levels of Sting (Fig. 3G; Supplementary Fig. S4D). Recent evidence suggests that high doses of IR upregulate Trex1 to break down cytoplasmic DNA and smother STING induction (35). Thus, we sought to determine whether Trex1 is induced by 20-Gy IR so that we did not observe IFN-I upregulation. We treated MOC2-E6/E7 cells with 5-Gy, 10-Gy, and 20-Gy IR, and found that mRNA levels of *Trex1 and Ifnb1* remain stable (Supplementary Fig. S4E and S4F). Then, we treated tumor-bearing mice with 3 fractionated doses of 8-Gy or a single dose of 20-Gy IR, and consistently found that neither treatment upregulates *Trex1* (Supplementary Fig. S4G). Collectively, although IR does not induce immune activation in this tumor model, Sox2 significantly reduces intrinsic IFN-I signaling in the TME.

Next, we explored whether Sox2-mediated IFN-I suppression negatively affects tumor-homing of the effectors and found that the infiltration of CD3$^+$CD8$^+$ T cells is significantly inhibited in Sox2-positive tumors (Fig. 3H). Notably, similar to human HNSCC (36), the CD8$^+$ T cells in the mouse TILs contain a significantly higher PD-1^{high} population than the peripheral, suggesting a state of exhaustion (Supplementary Fig. S4H; ref. 37). To validate whether Sox2-mediated growth advantage is indeed dependent on its suppression of IFN-I signaling in the TME, we implanted control and Sox2-expressing tumors into IFN-I receptor *Ifnar1*-deficient hosts. No difference in tumor growth is detected between the two groups (Fig. 3I). In agreement, the expression levels of IFN-I downstream target genes, such as *Cxcl9*, *Cxcl10*, and *Mx1*, are comparable between the groups (Fig. 3J–L).

To characterize the pathologic correlation of SOX2 expression in human disease, we first generated tissue microarrays (TMA) that contain 195 primary HNSCC patients with 3 cores for each

patient. We found that SOX2 expression levels are significantly higher in patients with advanced stage HNSCC and lymph node metastasis (Fig. 3M and N; Supplementary Table S2). Given that nodal metastasis is associated with HPV status, we further analyzed gene expression data from 519 HNSCC specimens in the TCGA and found that *SOX2* expression levels are higher in HPV$^+$ patients (Supplementary Fig. S5A). Because nodal status and clinical stage may not entirely depend on immune cell infiltration in the clinical specimens, we took a more direct approach to characterize the impact of SOX2 on TILs. We resolved the immune landscape of 519 HNSCC specimens by calculating the percentages of each immune cell subset using a machine learning tool CIBERSORT (20), and found that tumors expressing high levels of Sox2 harbor increased regulatory T cells and decreased M1-like macrophages (Supplementary Fig. S5B), both of which dampen tumor-specific effector responses.

Nanosatellites enhance the potency of STING agonist

Decreased IFN-I signaling in the TME hampers the recruitment and M1-like polarization of APC, which in turn limits its antigen processing, maturation, and cross-priming functions. To restore APC function and deliver high-density tumor-specific antigens for the expansion of tumor-specific CD8$^+$ CTLs, we developed a novel nanosatellite vaccine SatVax, which is engineered to promote the intracellular delivery of the STING agonist cGAMP as an adjuvant and enhance tumor antigen 3D density. Nanosatellites feature a biodegradable polysiloxane-containing polymer-coated iron oxide core (IONP) with inert gold (Au) satellites (Fig. 4A). The core-satellite structure further increases surface area for vaccine delivery. The hydrodynamic size of nanosatellite measures 80 nm, and conjugation with peptides and cGAMP increases its size to about 100 nm (Fig. 4B). Nanosatellite promotes cGAMP-induced ISRE activity in a monocytic cell line THP-1 cells (Fig. 4C). Nanosatellite significantly improves the intracellular delivery of cGAMP and IFN-I signaling, as evidenced by higher mRNA levels of *IFNA4*, *IFNB1*, *ISG15*, *ISG54*, *CXCL9*, and *CXCL10* in the presence of nanosatellites (Fig. 4D–I). To measure the intracellular uptake of antigens, we labeled the E7 peptides with a FAM fluorophore and incubated the peptides with primary bone marrow–derived macrophages. We found that nanosatellites significantly promote the intracellular uptake of the vaccine components (Fig. 4J). In agreement, when we challenged primary BMDCs with cGAMP in the absence or presence of nanosatellites, we found that nanosatellites enhance the expression levels of MHC Class II molecule and CD86, suggesting improved APC maturation (Fig. 4K and L).

## The nanosatellite vaccine SatVax (R9F, Q15L) improves tumor-specific immunity

To examine whether SatVax is able to travel to the lymph nodes where the APCs can present the antigens and activate CD8$^+$ T cells, we performed MRI to trace SatVax by T2* relaxation. We found that SatVax rapidly accumulates in the inguinal and popliteal lymph nodes after subcutaneous injections (Fig. 5A). In our initial formulation, we included two antigenic peptides—a 9 amino-acid core epitope of E7 (R9F) and E6 Q15L. By administering subcutaneous injections of SatVax (R9F, Q15L) at a distant site once per week for 3 weeks, we significantly reduced tumor burden in C57BL/6 hosts (Fig. 5B). After the tumors were harvested 25 days postimplantation, RNA was extracted to examine IFN-I transcripts. SatVax (R9F, Q15L) potently promotes the
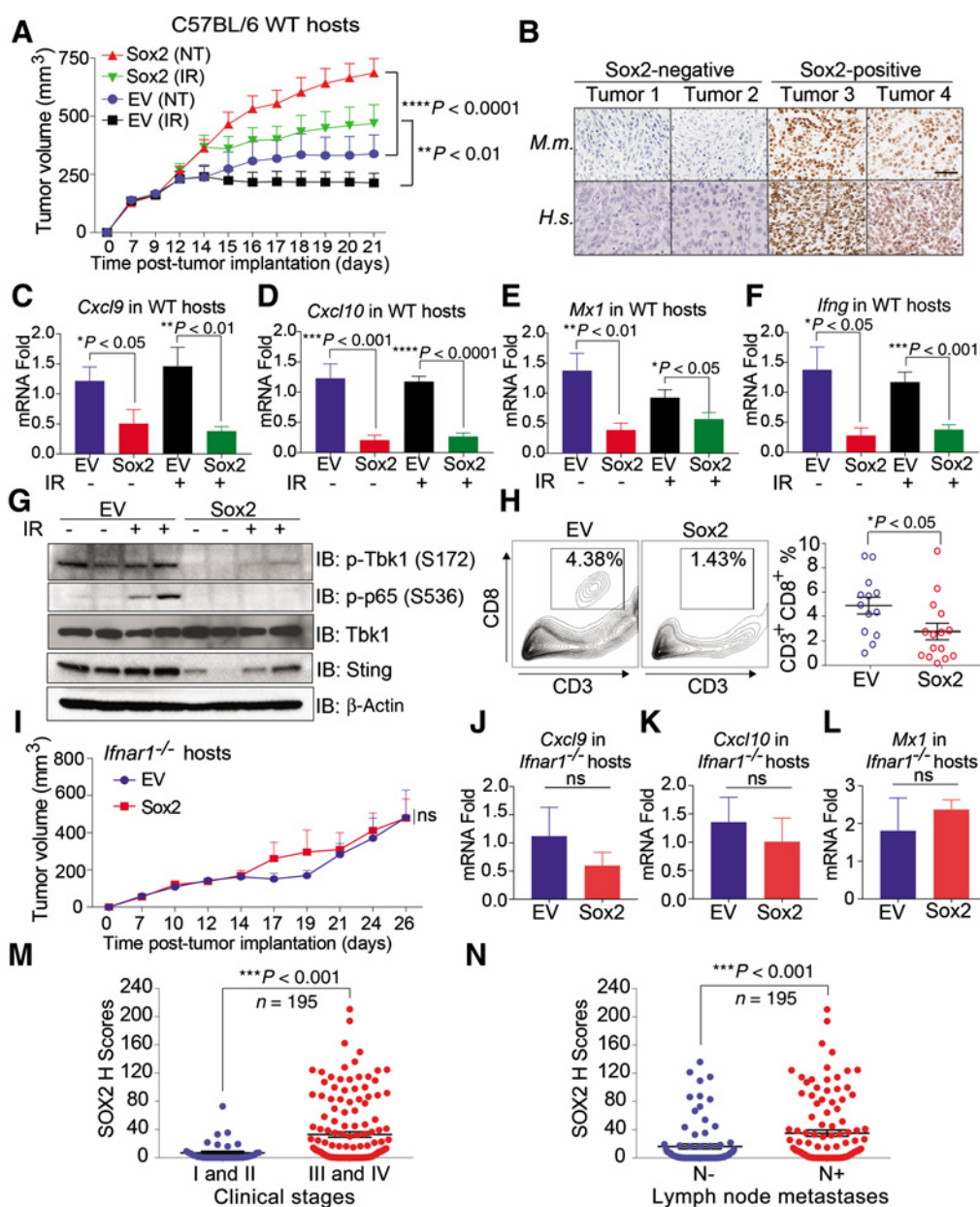
Figure 3.
Sox2 promotes tumor growth *in vivo* and potentiates an immunosuppressive microenvironment. **A,** One million EV control or Sox2-expressing MOC2-E6/E7 cells were implanted subcutaneously in C57BL/6 mice. A 20-Gy IR was administered on day 14 posttumor implantation. Results represent mean ± SEM, $n = 8$ for each group from two independent repeats. Comparisons were made using two-way ANOVA, followed by multiple comparisons test. **B,** IHC staining of SOX2 expression in grafted MOC2-E6/E7 tumors (top) and primary human HNSCC specimens (bottom). M.m. *Mus musculus*; H.s. *Homo sapiens*. Scale bar, 50 μm. **C–F,** Tumors were harvested and homogenized for RNA extraction. Tc1/Th1 activation marker genes, *Cxcl9, Cxcl10, Mx1*, and *Ifng*, were quantitated by qPCR ($n = 4$ with for each group with technical triplicates for each sample). Comparisons between two groups were made using two-way ANOVA followed by multiple comparisons test. Results represent mean ± SEM. **G,** Representative immunoblots of tumor homogenates are shown to assess the activation of IFN-I signaling. Densitometric analysis is shown in Supplementary Fig. S4B–S4D. **H,** TILs were separated using Ficoll-paque gradient, and the frequency of CD3$^+$ CD8$^+$ population was quantitated by flow cytometry. Comparisons between two groups were made using unpaired two-tailed *t* test. Results represent mean ± SEM. Each open circle represents TILs from one mouse. $n = 13$ for EV, $n = 15$ for Sox2. **I,** A total of 1×10^6 EV control or Sox2-expressing MOC2-E6/E7 cells implanted subcutaneously in *Ifnar1*$^{-/-}$ mice ($n = 4$ in each group with 2 repeats). A Generalized Estimating Equations (GEE) model was employed to compare the growth curves ($P = 0.5$). ns, nonsignificant. **J–L,** Tumors from **I** were harvested and homogenized for RNA extraction. qPCR was performed for *Cxcl9, Cxcl10* and *Mx1. n = 4* for each group. Results represent mean ± SEM, qPCR was performed in triplicates; ns, nonsignificant. **M** and **N,** Primary HNSCC specimens from 195 patients were procured and made into the TMAs, which were stained with anti-SOX2 antibody. The expression levels of SOX2 within the tumor cells were assessed by Aperio ImageScope, and compared among different patient groups using the Wilcoxon rank-sum test. The IHC score for any given specimen was determined by averaging the scores of 3 cores, and the cores that do not contain sufficient tumor material were omitted from the analysis. Each dot represents a patient sample, mean ± SEM, $n = 195$. Demographic information for HNSCC samples is reported in Supplementary Table S2.
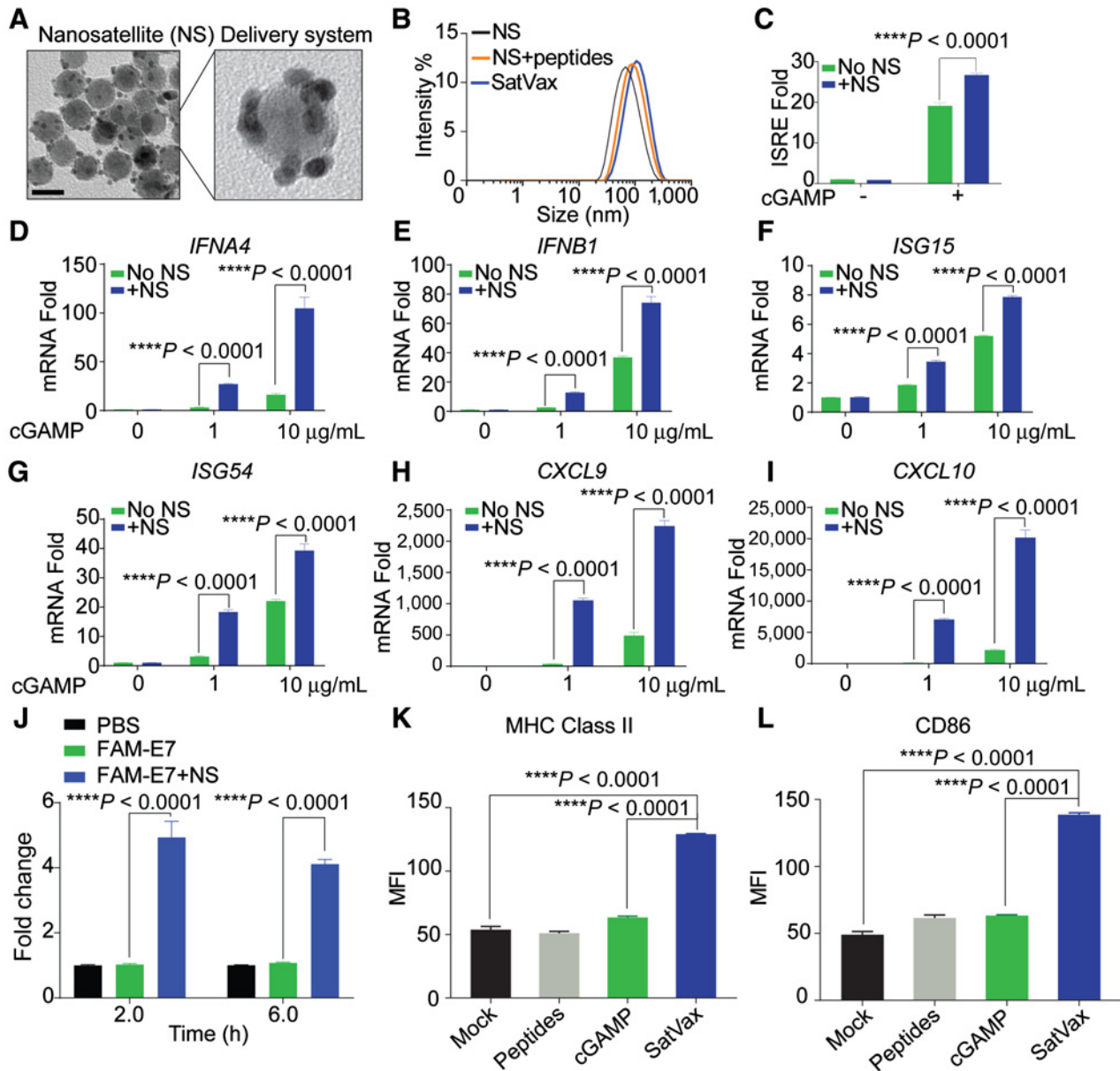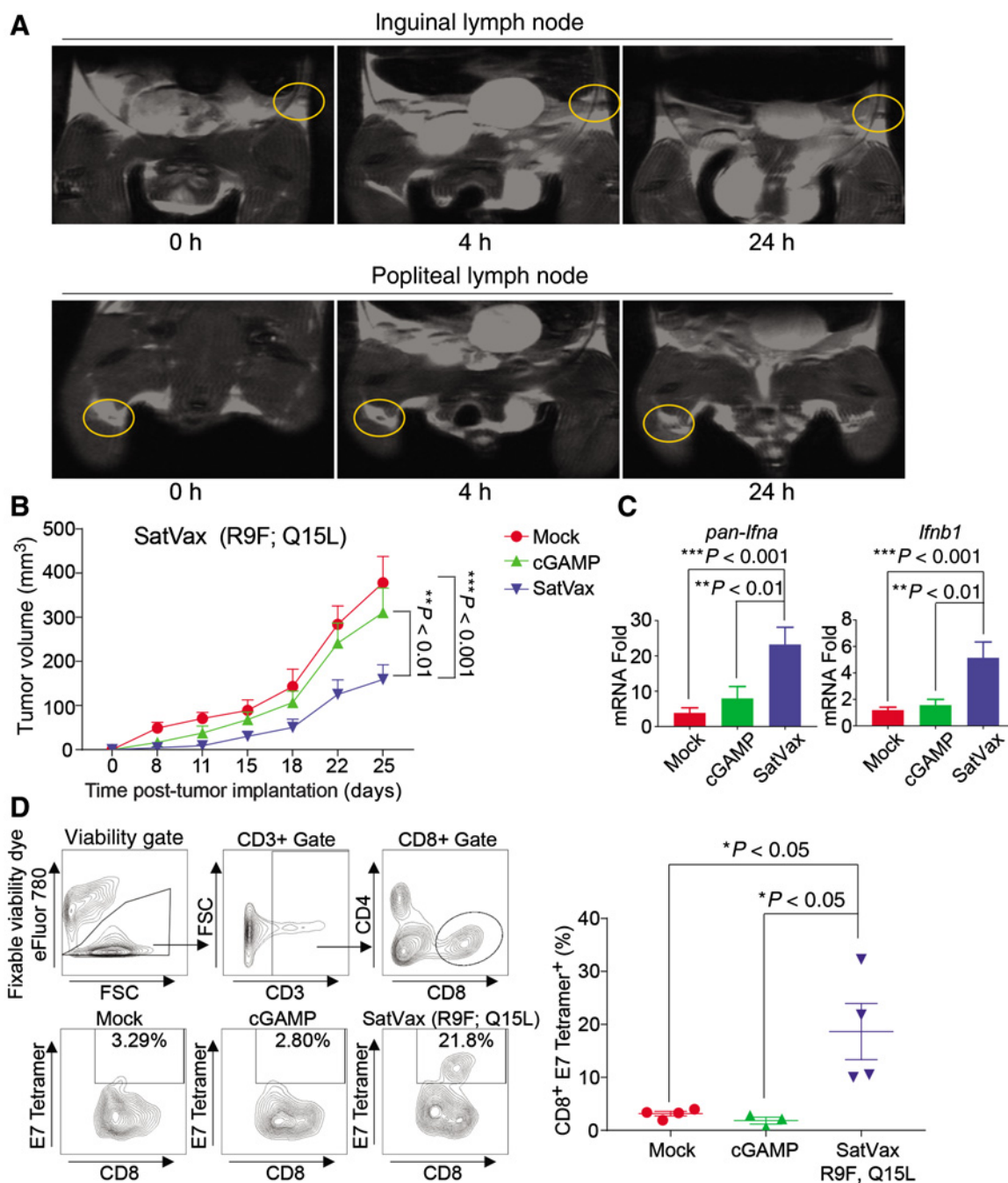
Figure 4.
Nanosatellite enhances the potency of STING agonist. **A,** Transmission electron microscopy of the core-satellite structure was performed. Scale bar, 20 nm. **B,** Normal distribution of the nanosatellite hydrodynamic diameters prior to and after peptides/cGAMP conjugation is shown. **C,** THP1-Blue ISG cells, which express a secreted embryonic alkaline phosphatase (SEAP) reporter, were challenged with cGAMP in the absence or presence of the nanosatellite delivery vehicle for 16 hours. IFN-regulatory factor activity was quantitated by measuring SEAP activity. Results represent mean ± SEM of three biological replicates. **D–I,** THP1 cells were treated with different doses of cGAMP, with or without the nanosatellite delivery vehicle for 16 hours. The mRNA abundance of the indicated IFN-I signaling genes were quantitated by qPCR. Results represent mean ± SEM of three biological replicates. Two-way ANOVA with Bonferroni posttest was performed for statistical analysis. **J,** Primary bone marrow–derived macrophages were incubated with FAM-labeled peptides with or without NS for 2 or 6 hours. Intracellular uptake was measured by FAM fluorescence intensity. Results represent mean ± SEM of three biologic replicates. **K** and **L,** Primary bone marrow–derived dendritic cells were treated with peptides, cGAMP, or SatVax for 48 hours. Dendritic cells maturation markers, such as MHC class II and CD86 were analyzed by flow cytometry. Median fluorescence intensity (MFI) was plotted for each marker. Results represent mean ± SEM of three biologic replicates. Data were analyzed by one-way ANOVA, followed by multi-comparisons posttest.

production of *pan-Ifna* and *Ifnb1* (Fig. 5C). In contrast, cGAMP alone shows modest effect at this late time point, probably due to insufficient intracellular delivery and rapid degradation *in vivo* (Fig. 5C). To validate whether SatVax (R9F, Q15L) stimu-lates the production of tumor-specific CTL, we stained TILs with a tetramer recognizing H-2D^b-restricted HPV16 E7 epitope RAHYNIVTF. Vaccine-treated group shows an over 10-fold increase of E7-specific CD8$^+$ CTLs (Fig. 5D).

Figure 5.
SatVax (R9F; Q15L) accumulates in the lymph nodes and promotes tumor-specific immunity. **A,** Magnetic resonance imaging of inguinal lymph node and popliteal lymph node regions (circled) of C57BL/6 mouse at 4 hours and 24 hours postinjection of SatVax (R9F; Q15L) was performed using TE = 30 ms and TR = 4,000 ms. The mice were imaged before the subcutaneous administration of SatVax at tail base as self-control. **B,** Tumor growth was monitored in C57BL/6 mice treated with SatVax formulation containing a core E7 epitope (R9F) and an E6 peptide (Q15L; injected subcutaneously at tail base once per week for three weeks), or cGAMP. Results represent mean ± SEM, $n = 4$ in each group. Two-way ANOVA with posttest was performed. **C,** Total RNA was extracted from tumor homogenates and assessed for the transcripts of *pan-Ifna* and *Ifnb1*. Results represent mean ± SEM, $n = 4$ per group, qPCR was performed in triplicates. Comparisons were made using one-way ANOVA followed by multiple comparisons test. **D,** TILs were separated using Ficoll-Paque gradient, and a representative contour plot of viable TILs is shown (left). The E7-specific CTL were quantitated by flow cytometric analysis of H-2D^b-restricted RAHYNIVTF-specific tetramer staining (right). One sample was excluded in the cGAMP group due to inadequate number of TILs. Results represent mean ± SEM ($n = 4$ per group).

SatVax (Q19D, Q15L) improves survival and the efficacy of ICR blockade

As longer peptides may increase the electrostatic interaction–based cGAMP condensation and protect the core epitope from rapid degradation, we next manufactured a SatVax formulation that contains E6 Q15L and a longer E7 peptide Q19D, which was used in HPV peptide vaccines (38). Three weekly subcutaneous injections of SatVax (Q19D, Q15L) were administered at tail base with the first dose given on day 3. The same amount of peptides, cGAMP, and six intraperitoneal injections of 100 μg anti-PD-L1 were given as controls. SatVax (Q19D, Q15L) significantly reduces tumor burden with superior therapeutic efficacy to that of cGAMP alone ($P < 0.001$; Fig. 6A). SatVax (Q19D, Q15L) significantly extends host survival ($P = 0.00025$; Fig. 6B). In agreement, SatVax (Q19D, Q15L)-treated mice demonstrate the best IFN-I induction, as shown by the highest transcript levels of pan-Ifna and Ifnb1 (Fig. 6C and D). Flow cytometric analysis of TILs shows that SatVax (Q19D, Q15L) expands E7-specific CD8$^+$ CTL for over 12-fold, contributing to its therapeutic efficacy (Fig. 6E). To further evaluate the efficacy SatVax, we delayed our vaccine administration until our tumors reached about 200 mm^3, and compared it with a peptide vaccine emulsified in one of the strongest clinical vaccine adjuvants montanide (39). We found that SatVax more effectively controls tumor growth and improves host survival (Supplementary Fig. S6A and S6B).

The CD8$^+$ CTL in the TME exhibits significantly higher expression levels of PD-1 (Supplementary Fig. S4H), suggesting a state of exhaustion (37). To prevent vaccine-induced CTL rapidly entering into exhaustion, we combined SatVax (Q19D, Q15L) with anti-PD-L1 to treat the more aggressive Sox2-positive tumors (Fig. 6F; Supplementary Fig. S7A). Because of the aggressive tumor growth, we reduced the cell number that we used in Fig. 3A to prevent mouse lethality in the mock control group prior to the completion of the treatment schedule. We found that a combination of SatVax with anti-PD-L1 demonstrates superior efficacy to either single treatment in suppressing tumor growth and extending host survival (Fig. 6F and G). In fact, 4 of 5 mice that were treated with SatVax and anti-PD-L1 achieved a completely tumor-free state for 18 days posttumor implantation (Supplementary Fig. S7B). Both SatVax and SatVax with anti-PD-L1 treatments significantly expand the E7-specific CD8$^+$ CTL repertoire (Fig. 6H). Notably, the combination of SatVax and anti-PD-L1 leads to over 86% reduction in the CD8$^+$ PD-1^{high} CTL and 50% reduction in CD8$^+$ Tim3$^+$ populations (Fig. 6I and J), both of which show functional exhaustion (37, 40).

Discussion

Squamous cell carcinomas are in general less immunogenic than melanomas. Only 13.3% of the HNSCC patients responded to anti-PD-1 (4), while 33% of the melanoma patients showed response to anti-PD-1 (41). But our understanding of the mechanism underpinning the hypoimmunogenicity of HNSCC remains very limited. Effector immune cell-mediated IFN-γ signaling is preceded by proper tumor-homing and maturation of APC, which requires the expression of IFN-I signatures. In this study, we identified the DNA-sensing signaling as a pivotal pathway modulating HNSCC sensitivity to immune killing (Fig. 1). We characterized how a frequently amplified HNSCC oncogene, SOX2 (25, 29, 42), potentiates tumor immune suppression by inhibiting the STING-mediated IFN-I activation (Figs. 2 and 3). SOX2 has a known function in promoting cancer "stemness". Cancer stem cells are more resistant to chemoradiotherapy, and exhibit immunosuppressive effect (43). This study reveals a previously unknown mechanistic link between SOX2 and an immunosuppressive TME. Previous studies including ours suggest that autophagy serves as a critical checkpoint for IFN-I activation (17). The cGAS-STING DNA-sensing pathway is a known cargo for autophagosomes (31, 44). We found that SOX2 promotes autophagic flux, inhibition of which restores STING expression (Fig. 2I). These results reveal a critical oncogenic pathway that inhibits the immunogenicity of HNSCC by targeting STING signaling.

Although IR has proven an immune-priming strategy in several tumor models, we found that IR does not activate STING-mediated anti-tumor immunity in our model. It is less likely due to IR-induced Trex1-mediated cytoplasmic DNA degradation, as we found that neither single dose nor fractionated low-dose IR upregulates Trex1. HPV E7 can specifically inhibit STING (45), which may explain why we did not observe IR-induced immunity in this model. Whether IR can efficiently expand intratumoral effectors and break resistance to ICR blockade in patients with HPV$^+$ HNSCC remains to be examined. However, Sox2 reduces intratumoral CD8$^+$ T-cell infiltration and encourages tumor growth in vivo regardless of IR (Fig. 3A). Sox2 has other functions including promoting cancer stemness. To ensure this phenotype we saw depends on the IFN-I pathway, we demonstrated that Sox2-mediated tumor growth advantage was diminished when we implanted tumors in Ifnar1$^{-/-}$ hosts, further supporting the role of Sox2–IFN-I axis in HNSCC immune escape (Fig. 3I–L). IFN-I drives the production of Th1 chemokines, which promotes M1-like polarization of APCs and eventually a favorable "T-cell–inflamed" TME. We deconvolved the immune landscape of HNSCC and found that SOX2 is associated with increased Tregs and decreased M1-like polarized macrophages (Supplementary Fig. S5B), a phenotype consistent with an IFN-deprived TME. This SOX2-IFN-I axis is not the only pathway which drives tumor immune escape; other pathways such as the Hippo pathway which inhibits IFN-I and antitumor immunity has been discovered recently (46). Thus, further exploration of mechanisms targeting the STING pathway will better delineate the HNSCC immune escape strategies.

To bypass HNSCC hypoimmunogenicity and expand the tumor-specific CTL repertoire, we engineered a novel nanosatellite vaccine delivery system that significantly enhances the potency of STING agonist and delivers high-density tumor antigens. We show that the nanosatellite vaccine SatVax significantly increases antigen intracellular uptake and improves APC maturation (Fig. 4). The vaccine rapidly accumulates in the lymph node and shows robust protection of the hosts (Figs. 5 and 6). It potently improves IFN-I signaling in the TME in vivo and expands the tumor-specific CD8$^+$ CTL in the tumors over 12-fold (Figs. 5 and 6). Although cancer vaccines are particularly attractive in a "minimal disease" setting after definitive surgical debulking to prevent recurrence and deescalate treatment, they are not meant to be used as a standalone approach. We found that SatVax improves tumor-specific T-cell infiltration, which further benefits from an ICR blockade regimen to prevent them from rapidly entering into an exhaustion state. In fact, a combination of SatVax with anti-PD-L1 not only expands the effectors, but also significantly reduces the percentages of PD-1^{high}
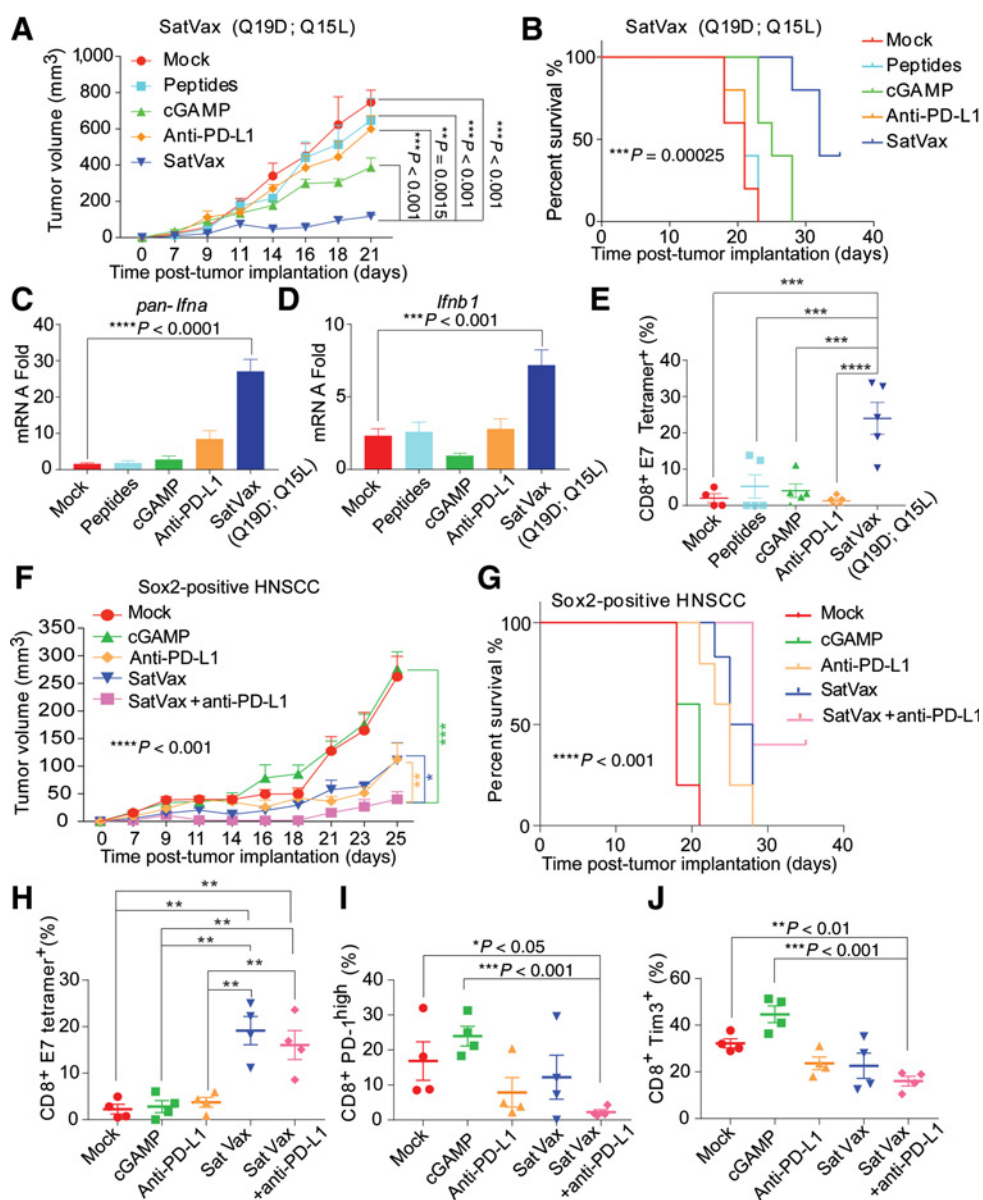
Figure 6.
SatVax (Q19D; Q15L) delivers significant protection against control and Sox2-expressing squamous cell carcinomas. **A,** The SatVax formulation with an extended antigenic peptide Q19D was subcutaneously administered once per week for three weeks after implantation of MOC2-E6/E7 tumor. The same amounts of peptides and cGAMP as in the vaccine formulation were injected as controls. Six doses of 100 μg anti-PD-L1 intraperitoneal injections were administered as a control. Tumor volumes were recorded on the indicated time points. Results represent mean ± SEM, n = 5 per group. A GEE model was employed to compare the growth curves among different treatment groups. The overall difference among groups is significant with a P <0.001. The P values for multicomparisons between any two groups are shown in Supplementary Table S3. **B,** Kaplan–Meier survival curves were plotted for all groups, n = 5 for each group. Log-rank (Mantel–Cox) test was performed for comparisons of survival curves. **C** and **D,** mRNA of pan-Ifna and Ifnb1 from each tumor were quantitated by qPCR. Results represent mean ± SEM, n = 5 in triplicates. Comparisons were made using one-way ANOVA followed by Tukey multiple comparisons test. **E,** TILs were analyzed by flow cytometry, and gated on CD3 and CD8, then analyzed for the frequency of H-2D^b–restricted RAHYNIVTF-specific T cells using E7-specific tetramer staining. Comparisons were made using one-way ANOVA followed by Tukey multiple comparisons test. ***, P < 0.001; ****, P < 0.0001. Each symbol represents TILs from one mouse. Results represent mean ± SEM, n = 5 per group. **F,** Growth of Sox2-expressing MOC2-E6/E7 tumors in the back of the neck were monitored. SatVax or cGAMP were administered subcutaneously at tail base once per week for 3 weeks. Intraperitoneal injections of 100 μg anti-PD-L1 were given twice per week for 3 weeks. The treatment schedule is shown in Supplementary Fig. S7A. Results represent mean ± SEM, n = 5 mice for each group. GEE was employed to compare the growth curves among different treatment groups. The overall difference among groups is significant with a P <0.001. The P values for multicomparisons between any two groups are shown in Supplementary Table S4. **G,** Kaplan–Meier survival curves of mice in **F** were plotted for all groups, n = 5 for each group. Log-rank (Mantel–Cox) test was performed for comparisons of survival curves. **H,** TILs from **F** were separated using Ficoll–paque gradient, and analyzed by flow cytometry. Viable TILs were gated on CD3 and CD8, and then analyzed for the frequency of E7-specific T cells using an H-2D^b–restricted RAHYNIVTF-specific tetramer staining. Each symbol represents TILs from one mouse. n = 4 in each group, mean ± SEM. **I** and **J,** Viable CD3^+ TILs were further analyzed for frequencies of CD8^+ PD-1^high and CD8^+ TIM3^+ cells. Comparisons were made using unpaired two-tailed t tests. Each symbol represents TILs from one mouse, n = 4 in each group, mean ± SEM (*, P < 0.05; **, P < 0.01; ***, P < 0.001).

CD8$^+$ CTL and Tim3$^+$CD8$^+$ CTL (Fig. 6I and J), both of which are functionally exhausted in HNSCC (40).

An ideal therapeutic vaccine is highly immunogenic, safe, consistent in quality, and off-the-shelf (5). The strengths of the nanosatellite delivery system include its efficacy, high-density tumor antigens, enhanced intracellular delivery of STING agonist, consistent quality control, and biocompatibility. Although SatVax in this report targets two antigenic peptides (bivalent), this system is amenable to incorporating any neoantigen peptides for further expansion of CD8$^+$ CTL repertoire. MOC2-E6/E7 C57BL/6-syngeneic tumors prove a unique model to test therapeutic HPV$^+$ cancer vaccines. Future work including the development of new immunocompetent HNSCC models, such as HPV-driven cancer model (47), and testing formulations in multiple models would help advance HNSCC vaccines. Overall, our work bridges a main knowledge gap by illuminating a novel HNSCC immune escape mechanism and developing a robust nanovaccine technology for cold cancers.

Disclosure of Potential Conflicts of Interest

P.J. Polverini is a consultant/advisory board member for Forsyth Institute. R.L. Ferris reports receiving commercial research grants from AstraZeneca/Medimmune, Bristol-Myers Squibb, Tesaro, and VentiRx Pharmaceuticals. No potential conflicts of interest were disclosed by the other authors.

Authors' Contributions

Conception and design: Y.S. Tan, K. Sansanaphongpricha, Q. Chen, R.L. Ferris, D. Sun, Y.L. Lei
Development of methodology: Y.S. Tan, K. Sansanaphongpricha, R.L. Ferris, Y.L. Lei

Acquisition of data (provided animals, acquired and managed patients, provided facilities, etc.): Y.S. Tan, K. Sansanaphongpricha, C.R. Donnelly, X. Luo, B.R. Heath, X. Zhao, R.L. Ferris, G. Wolf, Y.L. Lei
Analysis and interpretation of data (e.g., statistical analysis, biostatistics, computational analysis): Y.S. Tan, K. Sansanaphongpricha, Y. Xie, C.R. Donnelly, B.R. Heath, X. Zhao, E.L. Bellile, R.L. Ferris, G. Wolf, Y.L. Lei
Writing, review, and/or revision of the manuscript: Y.S. Tan, K. Sansanaphongpricha, C.R. Donnelly, P.J. Polverini, S. Young, T.E. Carey, J.E. Nör, R.L. Ferris, G. Wolf, D. Sun, Y.L. Lei
Administrative, technical, or material support (i.e., reporting or organizing data, constructing databases): B.R. Heath, R.L. Ferris, G. Wolf, Y.L. Lei
Study supervision: R.L. Ferris, Y.L. Lei
Other (providing related information): H. Hu
Other (providing nanosatellite materials for the study): H. Chen

The costs of publication of this article were defrayed in part by the payment of page charges. This article must therefore be hereby marked *advertisement* in accordance with 18 U.S.C. Section 1734 solely to indicate this fact.

References

1. Yom SS, Mallen-St Clair J, Ha PK. Controversies in postoperative irradiation of oropharyngeal cancer after transoral surgery. Surg Oncol Clin N Am 2017;26:357–70.
2. Maxwell JH, Grandis JR, Ferris RL. HPV-associated head and neck cancer: unique features of epidemiology and clinical management. Annu Rev Med 2016;67:91–101.
3. Bauman JE, Cohen E, Ferris RL, Adelstein DJ, Brizel DM, Ridge JA, et al. Immunotherapy of head and neck cancer: emerging clinical trials from a National Cancer Institute Head and Neck Cancer Steering Committee Planning Meeting. Cancer 2017;123:1259–71.
4. Ferris RL, Blumenschein G Jr, Fayette J, Guigay J, Colevas AD, Licitra L, et al. Nivolumab for recurrent squamous-cell carcinoma of the head and neck. N Engl J Med 2016;375:1856–67.
5. Tan YS, Sansanaphongpricha K, Prince MEP, Sun D, Wolf GT, Lei YL. Engineering vaccines to reprogram immunity against head and neck cancer. J Dent Res 2018;97:627–34.
6. Polverini PJ, D'Silva NJ, Lei YL. Precision therapy of head and neck squamous cell carcinoma. J Dent Res 2018;97:614–21.
7. Zitvogel L, Galluzzi L, Kepp O, Smyth MJ, Kroemer G. Type I interferons in anticancer immunity. Nat Rev 2015;15:405–14.
8. Lei Y, Xie Y, Tan YS, Prince ME, Moyer JS, Nor J, et al. Telltale tumor infiltrating lymphocytes (TIL) in oral, head & neck cancer. Oral Oncol 2016;61:159–65.
9. Woo SR, Corrales L, Gajewski TF. Innate immune recognition of cancer. Annu Rev Immunol 2015;33:445–74.
10. Ishikawa H, Barber GN. STING is an endoplasmic reticulum adaptor that facilitates innate immune signalling. Nature 2008;455:674–8.
11. Sun L, Wu J, Du F, Chen X, Chen ZJ. Cyclic GMP-AMP synthase is a cytosolic DNA sensor that activates the type I interferon pathway. Science 2013; 339:786–91.
12. Peng D, Kryczek I, Nagarsheth N, Zhao L, Wei S, Wang W, et al. Epigenetic silencing of TH1-type chemokines shapes tumour immunity and immunotherapy. Nature 2015;527:249–53.
13. Fu J, Kanne DB, Leong M, Glickman LH, McWhirter SM, Lemmens E, et al. STING agonist formulated cancer vaccines can cure established tumors resistant to PD-1 blockade. Sci Transl Med 2015;7:283ra52.
14. Bullock TN, Mullins DW, Engelhard VH. Antigen density presented by dendritic cells in vivo differentially affects the number and avidity of primary, memory, and recall CD8+ T cells. J Immunol 2003;170:1822–9.
15. Zhao M, Sano D, Pickering CR, Jasser SA, Henderson YC, Clayman GL, et al. Assembly and initial characterization of a panel of 85 genomically validated cell lines from diverse head and neck tumor sites. Clin Cancer Res 2011;17:7248–64.
16. Andrade Filho PA, Lopez-Albaitero A, Gooding W, Ferris RL. Novel immunogenic HLA-A*0201-restricted epidermal growth factor receptor-specific T-cell epitope in head and neck cancer patients. J Immunother 2010;33:83–91.
17. Lei Y, Wen H, Yu Y, Taxman DJ, Zhang L, Widman DG, et al. The mitochondrial proteins NLRX1 and TUFM form a complex that regulates type I interferon and autophagy. Immunity 2012;36:933–46.
18. Lei Y, Kansy BA, Li J, Cong L, Liu Y, Trivedi S, et al. EGFR-targeted mAb therapy modulates autophagy in head and neck squamous cell carcinoma through NLRX1-TUFM protein complex. Oncogene 2016;35: 4698–707.
19. Sansanaphongpricha K, DeSantis MC, Chen H, Cheng W, Sun K, Wen B, et al. Multibuilding block janus synthesized by seed-mediated self-assembly for enhanced photothermal effects and colored brownian motion in an optical trap. Small 2017;13.
20. Gentles AJ, Newman AM, Liu CL, Bratman SV, Feng W, Kim D, et al. The prognostic landscape of genes and infiltrating immune cells across human cancers. Nat Med 2015;21:938–45.
21. Patel SJ, Sanjana NE, Kishton RJ, Eidizadeh A, Vodnala SK, Cam M, et al. Identification of essential genes for cancer immunotherapy. Nature 2017; 548:537–42.
22. Topham NJ, Hewitt EW. Natural killer cell cytotoxicity: how do they pull the trigger? Immunology 2009;128:7–15.

23. Rusinova I, Forster S, Yu S, Kannan A, Masse M, Cumming H, et al. Interferome v2.0: an updated database of annotated interferon-regulated genes. Nucleic Acids Res 2013;41 (Database issue):D1040–6.

24. Zhang L, Mo J, Swanson KV, Wen H, Petrucelli A, Gregory SM, et al. NLRC3, a member of the NLR family of proteins, is a negative regulator of innate immune signaling induced by the DNA sensor STING. Immunity 2014; 40:329–41.

25. Boumahdi S, Driessens G, Lapouge G, Rorive S, Nassar D, Le Mercier M, et al. SOX2 controls tumour initiation and cancer stem-cell functions in squamous-cell carcinoma. Nature 2014;511:246–50.

26. Lee SH, Oh SY, Do SI, Lee HJ, Kang HJ, Rho YS, et al. SOX2 regulates self-renewal and tumorigenicity of stem-like cells of head and neck squamous cell carcinoma. Br J Cancer 2014;111:2122–30.

27. Liu K, Jiang M, Lu Y, Chen H, Sun J, Wu S, et al. Sox2 cooperates with inflammation-mediated Stat3 activation in the malignant transformation of foregut basal progenitor cells. Cell Stem Cell 2013;12:304–15.

28. Siegle JM, Basin A, Sastre-Perona A, Yonekubo Y, Brown J, Sennett R, et al. SOX2 is a cancer-specific regulator of tumour initiating potential in cutaneous squamous cell carcinoma. Nat Commun 2014;5:4511.

29. The Cancer Genome Atlas Research Network. Comprehensive genomic characterization of head and neck squamous cell carcinomas. Nature 2015;517:576–82.

30. Guo H, Konig R, Deng M, Riess M, Mo J, Zhang L, et al. NLRX1 sequesters STING to negatively regulate the interferon response, thereby facilitating the replication of HIV-1 and DNA viruses. Cell Host Microbe 2016;19:515–28.

31. Konno H, Konno K, Barber GN. Cyclic dinucleotides trigger ULK1 (ATG1) phosphorylation of STING to prevent sustained innate immune signaling. Cell 2013;155:688–98.

32. Onken MD, Winkler AE, Kanchi KL, Chalivendra V, Law JH, Rickert CG, et al. A surprising cross-species conservation in the genomic landscape of mouse and human oral cancer identifies a transcriptional signature predicting metastatic disease. Clin Cancer Res 2014;20:2873–84.

33. Lei Y, Jaradat JM, Owosho A, Adebiyi KE, Lybrand KS, Neville BW, et al. Evaluation of SOX2 as a potential marker for ameloblastic carcinoma. Oral Surg Oral Med Oral Pathol Oral Radiol 2014;117:608–16.

34. Deng L, Liang H, Xu M, Yang X, Burnette B, Arina A, et al. STING-dependent cytosolic DNA sensing promotes radiation-induced type I interferon-dependent antitumor immunity in immunogenic tumors. Immunity 2014;41:843–52.

35. Vanpouille-Box C, Alard A, Aryankalayil MJ, Sarfraz Y, Diamond JM, Schneider RJ, et al. DNA exonuclease Trex1 regulates radiotherapy-induced tumour immunogenicity. Nat Commun 2017;8:15618.

36. Li J, Jie HB, Lei Y, Gildener-Leapman N, Trivedi S, Green T, et al. PD-1/SHP-2 inhibits Tc1/Th1 phenotypic responses and the activation of T cells in the tumor microenvironment. Cancer Res 2015;75:508–18.

37. Kansy BA, Concha-Benavente F, Srivastava RM, Jie HB, Shayan G, Lei Y, et al. PD-1 status in CD8(+) T cells associates with survival and anti-PD-1 therapeutic outcomes in head and neck cancer. Cancer Res 2017;77: 6353–64.

38. Bartkowiak T, Singh S, Yang G, Galvan G, Haria D, Ai M, et al. Unique potential of 4-1BB agonist antibody to promote durable regression of HPV+ tumors when combined with an E6/E7 peptide vaccine. Proc Natl Acad Sci U S A 2015;112:E5290–9.

39. Reuschenbach M, Pauligk C, Karbach J, Rafiyan MR, Kloor M, Prigge ES, et al. A phase 1/2a study to test the safety and immunogenicity of a p16 (INK4a) peptide vaccine in patients with advanced human papillomavirus-associated cancers. Cancer 2016;122:1425–33.

40. Shayan G, Srivastava R, Li J, Schmitt N, Kane LP, Ferris RL. Adaptive resistance to anti-PD1 therapy by Tim-3 upregulation is mediated by the PI3K-Akt pathway in head and neck cancer. Oncoimmunology 2017;6: e1261779.

41. Ribas A, Hamid O, Daud A, Hodi FS, Wolchok JD, Kefford R, et al. Association of pembrolizumab with tumor response and survival among patients with advanced melanoma. JAMA 2016;315:1600–9.

42. Bass AJ, Watanabe H, Mermel CH, Yu S, Perner S, Verhaak RG, et al. SOX2 is an amplified lineage-survival oncogene in lung and esophageal squamous cell carcinomas. Nat Genet 2009;41:1238–42.

43. Lee Y, Shin JH, Longmire M, Wang H, Kohrt HE, Chang HY, et al. CD44+ cells in head and neck squamous cell carcinoma suppress T-cell-mediated immunity by selective constitutive and inducible expression of PD-L1. Clin Cancer Res 2016;22:3571–81.

44. Saitoh T, Fujita N, Hayashi T, Takahara K, Satoh T, Lee H, et al. Atg9a controls dsDNA-driven dynamic translocation of STING and the innate immune response. Proc Natl Acad Sci U S A 2009;106: 20842–6.

45. Lau L, Gray EE, Brunette RL, Stetson DB. DNA tumor virus oncogenes antagonize the cGAS-STING DNA-sensing pathway. Science 2015;350: 568–71.

46. Moroishi T, Hayashi T, Pan WW, Fujita Y, Holt MV, Qin J, et al. The hippo pathway kinases LATS1/2 suppress cancer immunity. Cell 2016; 167:1525–39.

47. Callejas-Valera JL, Iglesias-Bartolome R, Amornphimoltham P, Palacios-Garcia J, Martin D, Califano JA, et al. mTOR inhibition prevents rapid-onset of carcinogen-induced malignancies in a novel inducible HPV-16 E6/E7 mouse model. Carcinogenesis 2016;37:1014–25.